

 Open access • Posted Content • DOI:10.1101/805473

## The Development, Function, and Plasticity of the Immune Macroenvironment in Cancer

— [Source link](#) 

Breanna M. Allen, Kamir J. Hiam, Cassandra E. Burnett, Anthony Venida ...+3 more authors

**Institutions:** University of California, Berkeley, Tel Aviv University

**Published on:** 16 Oct 2019 - bioRxiv (Cold Spring Harbor Laboratory)

**Topics:** Tumor microenvironment, Immune system and T cell

Related papers:

- [Tumor-host immune interactions and dendritic cell dysfunction.](#)
- [Role of immune system in tumor progression and carcinogenesis.](#)
- [Immunosuppression and Cancer](#)
- [Tumor resident regulatory T cells](#)
- [The Role of the Immune System and Immunoregulatory Mechanisms Relevant to Melanoma](#)

Share this paper:    

View more about this paper here: <https://typeset.io/papers/the-development-function-and-plasticity-of-the-immune-33jpmo9k59>

1  
2  
3  
4  
5  
6  
7  
8  
9  
10  
11  
12  
13  
14  
15  
16  
17  
18  
19  
20  
21  
22  
23  
24  
25  
26  
27

# The Development, Function, and Plasticity of the Immune Macroenvironment in Cancer

Breanna M. Allen<sup>1,2,5</sup>, Kamir J. Hiam<sup>1,2,5</sup>, Cassandra E. Burnett<sup>1,2</sup>, Anthony Venida<sup>1,3</sup>, Rachel DeBarge<sup>1,2</sup>,  
Yaron Carmi<sup>4</sup>, and Matthew H. Spitzer<sup>1,2\*</sup>

<sup>1</sup>Graduate Program in Biomedical Sciences, University of California, San Francisco, San Francisco, CA, USA

<sup>2</sup>Departments of Otolaryngology and Microbiology & Immunology, Helen Diller Family Comprehensive Cancer Center, Parker Institute for Cancer Immunotherapy, Chan Zuckerberg Biohub, University of California, San Francisco, San Francisco, CA, USA

<sup>3</sup>Department of Anatomy, University of California, San Francisco, San Francisco, CA, USA

<sup>4</sup>Department of Pathology, Sackler School of Medicine, Tel Aviv University, Tel Aviv, Israel.

<sup>5</sup>Co-First Author

\*Correspondence: [matthew.spitzer@ucsf.edu](mailto:matthew.spitzer@ucsf.edu) (M.H.S.)

28 **ABSTRACT**

29           Harnessing immune defense mechanisms has revolutionized cancer therapy, but our  
30 understanding of the factors governing immune responses in cancer remains incomplete, limiting patient  
31 benefit. Here, we use mass cytometry to define the organism-wide immune landscape in response to  
32 tumor development across five tissues in eight tumor models. Systemic immunity was dramatically  
33 altered across mouse models and cancer patients, with changes in peripheral tissues differing from those  
34 in the tumor microenvironment and taking place in phases during tumor growth. This tumor-experienced  
35 immune system mounted dampened responses to orthogonal challenges, including reduced T cell  
36 activation during viral or bacterial infection. Disruptions in T cell responses were not cell-intrinsic but  
37 rather due to reduced responses in antigen-presenting cells (APCs). Promoting APC activation was  
38 sufficient to restore T cell responses to orthogonal infection. All systemic immune changes were reversed  
39 with surgical tumor resection, revealing remarkable plasticity in the systemic immune state, which  
40 contrasts with terminal immune dysfunction in the tumor microenvironment. These results demonstrate  
41 that tumor development dynamically reshapes the composition and function of the immune  
42 macroenvironment.

43

44

45

46

47

48

49

50

## 51 MAIN TEXT

52 Exploiting the mechanisms of immune activation and suppression has rapidly expanded our  
53 toolkit against cancer, leading to diverse immunotherapeutic strategies and some impressive clinical  
54 results. The efficacy of immunotherapies is currently limited, however, to select cancer types and patient  
55 subsets, begging for a more thorough understanding of the factors that govern immune responses in  
56 cancer patients. The field has garnered a robust understanding of the changes within the tumor  
57 microenvironment (TME) that subvert immune surveillance and promote tumor growth. Heterogeneous  
58 populations of immunosuppressive myeloid cells dominate many local immune landscapes, largely acting  
59 to impede cytotoxic lymphocyte activity and survival<sup>1-4</sup>. Intratumoral cytotoxic CD8 T cells have been the  
60 focus of the vast majority of immunomodulatory strategies in cancer therapy. However, recent studies  
61 have demonstrated that cytotoxic T cells within the TME are highly and irreversibly dysfunctional,  
62 acquiring epigenetic programs that render them incapable of normal effector functions, such as  
63 proliferation, cytokine production, and cytolysis<sup>5</sup>. In parallel, we and others have found that systemic  
64 immune responses are an essential component of tumor-eradicating immunity<sup>6-10</sup>. Consistent with these  
65 results, activated T cells in human tumors after checkpoint blockade consist of clones not observed in the  
66 tumor before the onset of therapy<sup>11</sup>. These findings argue that initiating a *de novo* systemic anti-tumor  
67 immune response may be essential to achieving immunotherapeutic efficacy, especially in patients who  
68 lack a strong pre-existing T cell response to their tumor.

69 Despite evidence that a systemic response is required for cancer rejection, our understanding of  
70 how cancer development impacts the systemic immunity remains limited. Several lines of evidence  
71 suggest systemic immune perturbations in the presence of a tumor. Peripheral granulocytic and  
72 monocytic differentiation and expansion accompanies tumor progression<sup>12-14</sup>, including a reduction in the  
73 number of conventional dendritic cells in bone marrow and blood<sup>15</sup>. Systemic effects on lymphocytes  
74 remain poorly understood. Additionally, most studies have explored anti-tumor immune responses at a  
75 single, static time point, leaving the dynamicity of the immune system during cancer development an open  
76 question. A comprehensive definition of the tumor-experienced immune macroenvironment and how it  
77 emerges over disease progression remains a crucial avenue of investigation.

78 A plethora of immunotherapies and vaccines seek to elicit new immune responses in cancer patients,  
79 yet no consensus has emerged for the cellular and molecular requirements to achieve this goal. In other  
80 contexts, prior immune experience has important consequences for the response to new stimuli. Chronic  
81 infection and inflammation impact immune responsiveness to novel challenges by shifting basal cytokine  
82 levels, innate immune activation states, and overall lymphocyte composition<sup>16–18</sup>. A detailed assessment  
83 of how tumor burden impacts responses to secondary immune challenges has yet to be performed,  
84 despite the fact that many patients likely require new immune responses to benefit from  
85 immunotherapies. It is also unclear whether there are lasting immune impacts after successful primary  
86 tumor clearance. One study suggests that the accumulation of immunosuppressive myeloid cells in the  
87 spleen rapidly alleviates with tumor resection<sup>19</sup>, highlighting a dynamic interaction between tumor burden  
88 and immune state. Defining the functional capacity and stability of the tumor-experienced immune  
89 macroenvironment is critical for improving immunotherapies.

90 The advent of high content single-cell analysis and corresponding analytical methods now allows us  
91 to tackle the challenge of characterizing systems-level immune responses in cancer. Here, we defined  
92 the systemic immune landscape in response to tumor development across eight commonly used mouse  
93 models of cancer. These data, which are now publicly available, provide a rich resource for assessing  
94 the relevance of any model to a particular question of interest or tumor type. While each tumor has  
95 unique immunological consequences, we found that three distinct models of breast cancer converged on  
96 similar changes to the systemic immune state. Tumor burden led to dynamic shifts in the organization  
97 and functional capacity of immune cells across the organism, which culminated in attenuated responses  
98 to secondary immune challenges. Tumor resection was sufficient to revert the systemic immune  
99 landscape back to a healthy baseline. These findings have implications for how and when we apply  
100 immunomodulatory agents in cancer, emphasizing the importance of strategies that are informed by  
101 alterations in the immune macroenvironment.

102

### 103 **Systemic immune organization is altered across multiple tumor types**

104 We began by examining the TME across several commonly used mouse tumor models, which

105 spanned genetically-engineered and transplantable syngeneic models across different mouse strain  
106 backgrounds. We characterized a well-established, but pre-terminal tumor stage, to reflect the patient  
107 populations most often treated with immunotherapies, but also to avoid the confounding impact of end-of-  
108 life processes. When tumors reached approximately 1 cm<sup>3</sup> in volume, we harvested the tumor along with  
109 the blood, spleen, bone marrow, and tumor draining lymph node of each tumor-burdened animal and  
110 healthy control littermate. We utilized mass cytometry to quantify the abundance and activity state of  
111 immune cell subsets (Extended Data Table 1 and Extended Data Fig. 1) and performed principal  
112 component analysis (PCA) and Statistical Scaffold Mapping<sup>6</sup> to visualize and assess changes in immune  
113 cell abundances.

114         The immune composition of the TME was distinct between tumor types, varying in the degree of  
115 both immune infiltration and diversity (Fig. 1a and Extended Data Fig. 2a). The predominant immune cell  
116 types in many tumors were tumor-associated macrophages and other CD11b<sup>high</sup> myeloid subsets,  
117 particularly in the transplantable MC38 colorectal cancer and SB28 glioblastoma models. Interestingly,  
118 both transplantable LMP pancreatic cancer and genetically induced Braf<sup>T</sup>Pten melanoma models showed  
119 extensive eosinophil infiltration. B16-F10 syngeneic melanoma and three models of breast cancer  
120 (transplantable cell lines 4T1 and AT3, and genetically induced MMTV-PyMT) showed less relative  
121 abundance but much greater diversity in local immune cells, including B, T, and NK cell infiltration (Fig.  
122 1a and Extended Data Fig. 2a). The unique immune profiles across tumor types are reflected by PCA  
123 (Fig. 1b).

124         We next asked whether different tumors also resulted in distinct systemic immune landscapes.  
125 The immune compositions of the tumor draining lymph node, bone marrow, blood, and spleen were  
126 indeed altered, albeit to varying extents, across all tumor models (Fig. 1c). While varying in magnitude,  
127 the breast cancer models consistently shifted together across principal component (PC) 2 in the lymph  
128 node and PC1 in the bone marrow, blood, and spleen. Surprisingly, SB28 glioblastoma drove extensive  
129 and distinct shifts in systemic immunity despite its localization in the CNS. Alterations in immune  
130 composition in these peripheral sites did not correspond with local immune infiltrate. Thus, tumor burden  
131 consistently drives changes in peripheral immune organization, highly dependent on the identity of the

132 tumor and distinct from the patterns of immune infiltration in the TME.

133 We next performed Statistical Scaffold Analysis to interrogate the impact of tumor burden on  
134 individual immune cell types, focusing initially on the spleen as an example of a secondary lymphoid  
135 organ with immune responses initiated distal from the tumor (Fig. 1d and Extended Data Fig. 2b-f). Our  
136 approach enabled a detailed analysis of each major immune subset, building a complete picture of  
137 tumor-driven immune reorganization. All models exhibited expansions in the splenic myeloid  
138 compartment, which was dominant in some tumors, such as breast (Fig. 1d) but less dramatic in others,  
139 such as melanoma (Extended Data Fig. 2e-f). Extensive splenic remodeling in breast cancer was  
140 specifically characterized by relative increases in neutrophils, eosinophils, monocytes, and plasma cells  
141 and reductions of B and T cells (Fig. 1d). Again consistency was observed across breast cancer models,  
142 which span three mouse strain backgrounds (BALB/c for 4T1, C57BL/6 for AT3, and FVB/N for MMTV-  
143 PyMT), both orthotopic injection and spontaneous tumorigenesis, and a range of metastatic potential.  
144 Consistency despite these model differences argues strongly for a tumor and/or site-specific bias in  
145 systemic immune responses. In line with the mouse models, gene expression analysis of whole blood  
146 from untreated breast cancer patients and matched controls from the Norwegian Women and Cancer  
147 Study demonstrated a marked shift in the immune state (PC1 Wilcoxon rank sum p-value =  $5.0 \times 10^{-12}$ ,  
148 PC2 p-value =  $1.6 \times 10^{-6}$ ) (Fig. 1e). Cellular enrichment analysis demonstrated increases in neutrophils  
149 and plasma cells, as well as decreases in Th1 and CD8 T cells (Fig. 1f). Altogether, these data suggest  
150 that tumor burden broadly drives distinct immune macroenvironments, providing context to inform  
151 therapeutic manipulations designed to activate local versus systemic responses.

152

### 153 **Tumor growth drives non-linear changes in immune cell frequencies over time**

154 Tumors develop gradually, yet in the clinic tumors are sampled at one point in their development  
155 to provide prognostic information related to the immune response. To understand the dynamics that  
156 result in a given local and systemic immune response, we delved further into global immune remodeling  
157 over time. Given the pronounced and consistent systemic immune changes observed in breast cancer  
158 models, we focused on these tumor settings. We began our analysis of immune cell dynamics in an

159 orthotopic syngeneic model (4T1) due to its highly predictable kinetics before confirming results in an  
160 unrelated spontaneous model (MMTV-PyMT). We first asked whether tumor-driven immune changes  
161 developed discretely with tumor onset or progressively over tumor development. The absolute cell count  
162 of tumor-infiltrating leukocytes also positively correlated with tumor growth, supporting a progressive  
163 immune response (Extended Data Fig. 3a,  $r = 0.6$ ,  $p = 0.0256$ ). While absolute spleen cell counts  
164 increased along with spleen size during tumor development, cell frequencies as a percent of total  
165 leukocytes were comparable to absolute cell numbers per milligram of spleen tissue (Extended Data Fig.  
166 3b). Thus, cell frequency was illustrated as the primary measure. Deep profiling of both the tumor and  
167 splenic immune compositions by mass cytometry revealed nonparametric correlations in individual  
168 cluster frequencies with time (Fig. 2a-b), demonstrating at the single cell level that immune changes are  
169 indeed progressive. PCA of immune cell frequencies showed progressive changes across tissues over  
170 tumor growth in both 4T1 (Fig. 2c-d) and MMTV-PyMT tumors (Extended Data Fig. 3c). Importantly, the  
171 immune profile within the TME remained distinct from those observed in peripheral sites. The draining  
172 lymph node immune composition was unique, while coordinated changes were more apparent across the  
173 spleen, blood, and bone marrow. Neutrophil expansion in the spleen and bone marrow, culminating in  
174 elevated blood circulation, but lack of accumulation within the lymph node or tumor, is one feature  
175 contributing to these unique profiles (Fig. 2d).

176         Progressive systemic immune responses to tumor burden were not strictly linear. Rather, unique  
177 shifts in immune composition occurred at each analyzed time of tumor development. The magnitude of  
178 change was non-uniform between each time point as evident by the PCA (Fig. 2c and Extended Data  
179 Fig. 3c). While some population changes were relatively continuous, such as increasing neutrophils or  
180 decreasing  $CD4^+$  T cells, others were dynamic, like  $CD8^+$  T cells and Tregs, which reciprocally expanded  
181 and contracted at distinct times in the tumor and draining lymph node (Fig. 2d). To capture the behavior  
182 of more specific immune cell clusters over time, we constructed Statistical Scaffold maps comparing  
183 cluster abundances between each consecutive time point over 4T1 tumor growth (Extended Data Fig. 3d  
184 and Extended Data Fig. 4). In the spleen, expansion within the myeloid compartment began by day 7  
185 and continued to day 14, preceding the relative decline in the T and B cell compartments that became



186 evident by day 14 and continued through day (Extended Data Fig. 3d). The lymph node also showed the  
187 most dramatic immune changes by day 14 (Extended Fig. 4a), while changes in blood were more  
188 continuous (Extended Data Fig. 4b). The bone marrow and tumor contained less mature and clearly  
189 defined cell types, with many more inter-cluster connections and individualized patterns of change over  
190 tumor growth (Extended Data Fig. 4c-d). These data overwhelmingly demonstrate that the tumor immune  
191 response is a highly dynamic process.

192

### 193 **Immune cell states are dynamically altered across immune organs with tumor growth**

194 We were surprised by the dramatic alterations in T cells across tissues in the periphery, as the  
195 dominant mechanisms of T cell suppression in cancer are thought to occur only in tumor antigen-specific  
196 T cells as a consequence of chronic antigen exposure<sup>20</sup>, or as a consequence of local  
197 immunosuppression within the TME<sup>21</sup>. To understand the extent of these broader systemic impacts on T  
198 cells, we leveraged unsupervised cell clustering to identify changes in T cell subsets and cell states, as  
199 well as the potential coordination of responses across organs, during tumor growth. Because immune  
200 cell frequencies are compositional, we calculated the frequencies of individual T cell clusters as a  
201 percent of total T cells in each organ to distinguish changes in T cell composition from changes in other  
202 cell types. Dramatic changes in T cell subsets were observed at specific time points, including at an  
203 intermediate stage (day 14 for 4T1, 50mm<sup>2</sup> for MMTV-PyMT) and at a late stage (day 35 for 4T1,  
204 400mm<sup>2</sup> for MMTV-PyMT) (Fig. 3a, Extended Data Fig. 5a-b). Tissues contained both unique and shared  
205 T cell subsets that shifted with tumor growth (Fig. 3b-c, Extended Data Fig. 5c-e). The blood and spleen  
206 profiles were more similar and dominated by CD4<sup>+</sup> T cells. In contrast, the tumor T cell pool had more  
207 shared subsets with the bone marrow, including an increasing double negative T cell population and a  
208 decreasing NKT cell population with tumor progression (Fig. 3c).

209 Demonstrating the breadth of immune reorganization in cancer, all T cell clusters changed in  
210 abundance across multiple tissues between early and late disease time points (Fig. 3d). Of particular  
211 interest, tumor-infiltrating CD103<sup>+</sup> Tregs, described as potent suppressors of effector T cells<sup>22</sup>, were  
212 abundant at day 7 but decreased with tumor progression (Fig. 3e). This corresponded with CD103<sup>+</sup> Treg

213 expansion selectively in the draining lymph node, suggesting that distal suppressive mechanisms may  
214 support local changes to maintain a tumor-promoting systemic state. Anti-correlated changes extended  
215 to conventional CD4 T cells, where CD44<sup>+</sup> CD90<sup>high</sup> activated CD4 T cells decreased in the tumor but  
216 expanded in the lymph node (Fig. 3f). The spleen showed the greatest change in CD44<sup>+</sup> CD27<sup>+</sup> memory  
217 CD4<sup>+</sup> T cells, which decreased with disease progression (Fig. 3g). The blood showed expansion in  
218 activated CD44<sup>+</sup> CD4<sup>+</sup> T cells expressing the CD31 adhesion receptor, which can promote T cell survival  
219 in settings of inflammation (Fig. 3h)<sup>23</sup>. CD44<sup>+</sup> CD8<sup>+</sup> T cells expanding in lymph node expressed Ly6C  
220 (Fig. 3j), which can support lymph node homing of central memory T cells<sup>24</sup>. CD8<sup>+</sup> T cells generally  
221 expanded in the tumor, but the most dominant cluster expressed high levels of PD-1 and CD69  
222 previously associated with T cell dysfunction (Fig. 3i)<sup>25,26</sup>. To explore the extent of dysfunction, we  
223 interrogated intratumoral and splenic T cells for their expression of CD101 and CD38, two markers  
224 recently identified as evidence of permanent T cell dysfunction<sup>5</sup>. Late-stage tumor burden led to  
225 accumulation of CD38<sup>+</sup>CD101<sup>+</sup> CD8<sup>+</sup> T cells in the tumor as expected; however, this phenotype did not  
226 emerge in the spleen (Fig. 3k), suggesting that CD8<sup>+</sup> T cells are altered differently in the TME and in the  
227 periphery. Similar changes in T cell composition were observed in the MMTV-PyMT model (Extended  
228 Data Fig. 5c-h).

229 We ran a similar pan-organ clustering analysis for the mononuclear phagocyte subsets (Extended  
230 Data Fig. 6), and again found correlated and anti-correlated changes in cell states across sites with  
231 tumor progression. As expected, the tumor-infiltrating subsets were very distinct from peripheral subsets  
232 and expressed high levels of PD-L1.

233 We also specifically interrogated the expression dynamics of the PD-1 and PD-L1 immune  
234 checkpoint proteins, the most commonly manipulated pathway by cancer immunotherapies to facilitate T  
235 cell responses<sup>27</sup>. While expression of these molecules is used clinically for patient stratification, it  
236 remains unclear whether they are expressed consistently or modulated dynamically over time. We  
237 indeed found dynamic PD-1 and PD-L1 expression on infiltrating immune cells and non-immune cells of  
238 the TME (CD45<sup>-</sup> CD31<sup>-</sup>) for both 4T1 and AT3 breast cancer models (Extended Data Fig. 7a-b). Varied  
239 expression over time held true in peripheral lymphoid organs, particularly the spleen and blood

240 (Extended Data Fig. 7c). In fact, while the overall amount of PD-L1 expression was significantly less in  
241 the blood compared to the tumor, median leukocyte signal intensity was strongly positively correlated  
242 between these tissues (Extended Fig. 7d,  $r = 0.7487$ ,  $p = 0.001$ ). Both PD-1 and PD-L1 were  
243 promiscuously expressed across immune cell types, particularly within the TME (Extended Data Fig. 7e).  
244 The most prominent cells expressing PD-L1 in the periphery were non-classical monocytes<sup>28</sup> and cDCs,  
245 while PD-1 was abundantly expressed on T cells, neutrophils and eosinophils. Dynamicity in PD-1 and  
246 PD-L1 expression suggests the potential for differential sensitivity to checkpoint blockade over the  
247 course of tumor development.

248 One potential mechanism by which immune composition could be altered is a change in cellular  
249 proliferation or death rates. By assessing Ki67 expression, we discovered that immune proliferation  
250 indeed fluctuated systemically across breast cancer models (Extended Data Fig. 8a). Changes in  
251 proliferation were highly compartmentalized such that proliferation dynamics were unique to each site but  
252 coordinated across all immune cell subsets within that site (Extended Data Fig. 8a-d). We also measured  
253 the expression of cleaved Caspase-3 to assess cell death and observed only minor changes in the  
254 spleen (26 of 200 clusters changed significantly at day 14). Changes in Ki67 and cleaved caspase-3  
255 expression corresponded poorly with clusters that were increasing or decreasing in frequency in the  
256 spleen (Extended Data Fig. 8e). Thus, while tumor burden systemically alters proliferation and death,  
257 these processes alone likely do not account for the systemic immune alterations observed.

258

### 259 ***De novo* T cell responses are impaired by pre-existing malignancy**

260 Having established that tumor development drives an altered immune macroenvironment, we  
261 determined whether immune responses to new challenges would be affected. Type 1 immune responses  
262 are associated with strong cellular immunity and are generally thought to provide optimal anti-tumor  
263 immunity. As model systems to understand how type 1 immune responses might take place in the  
264 context of cancer, we challenged healthy or AT3 tumor-burdened mice with two well-described  
265 pathogens that induce potent type 1 immunity, including CD8<sup>+</sup> T cell proliferation and differentiation:  
266 lymphocytic choriomeningitis virus (LCMV) and *Listeria monocytogenes* (*Lm*)<sup>29,30</sup>. Tumor-burdened mice

267 still cleared the pathogens from the spleen (Fig. 4a-b), consistent with the lack of complete  
268 immunosuppression in solid tumor patients. However, the cellular immune response to infection was  
269 dramatically altered. The composition of CD8 T cells was significantly altered in tumor-burdened mice  
270 after infection, with marked reductions in short-lived and memory effector CD8 T cells (Fig. 4c). CD8<sup>+</sup> T  
271 cell proliferation was significantly abrogated under both infection conditions (Fig. 4d), along with impaired  
272 cytotoxic capacity indicated by a reduction in Granzyme B production (Fig. 4e). Because strong CD8<sup>+</sup> T  
273 cell responses are paramount to effective anti-tumor immunity, this impairment of new cellular immunity  
274 in the context of cancer presents a fundamental and unappreciated obstacle for immunotherapy.

275 We previously found that CD8<sup>+</sup> T cells with markers of terminal dysfunction were only observed  
276 in the TME and not the spleen (Fig. 3k). Consistent with this hypothesis, splenic CD8<sup>+</sup> T cells harvested  
277 from either control or tumor-burdened animals were equally capable of producing the key effector  
278 cytokines IFN $\gamma$ , TNF $\alpha$ , and IL-2 *in vitro* (Extended Data Fig. 9a). To test their functionality in the context  
279 of infection, CD8<sup>+</sup> T cells from OT-I transgenic mice expressing a high affinity T cell receptor specific for  
280 ovalbumin (SIINFEKL) were isolated from control or tumor-burdened mice. We confirmed that AT3  
281 tumors still drove systemic changes in TCR transgenic mice (Extended Data Fig. 9b). These cells were  
282 labeled with different fluorescent dyes to mark proliferation and were transferred together into healthy  
283 recipient mice immediately prior to infection with *Lm*-expressing ovalbumin. OT-I CD8<sup>+</sup> T cells from  
284 control and tumor-burdened mice proliferated equivalently (Fig. 5a). However, when OT-I T cells were  
285 transferred into tumor-burdened recipients prior to infection, they expanded poorly, failed to induce T-bet  
286 expression associated with differentiation into effector cells, and expressed elevated levels of PD-1 (Fig.  
287 5b). Similar results were also observed when polyclonal CD8 T cells from control or tumor-burdened  
288 mice were competitively transferred (Fig. 5c). These results demonstrate that cell extrinsic mechanisms  
289 suppress systemic T cell activation and function in the tumor context. Importantly, they also suggest that  
290 T cell behavior *in vitro* may not accurately predict their behavior once introduced into a tumor-burdened  
291 host, bearing implications for adoptive T cell therapies.

292 Since tumor-experienced CD8<sup>+</sup> T cells in the periphery were not dysfunctional, we hypothesized  
293 that impaired APC activity earlier during the course of infection may contribute to decreased peripheral

294 CD8<sup>+</sup> T cell activation. Dendritic cells (DCs) play a key role in orchestrating CD8<sup>+</sup> T cell responses to  
295 *Lm*<sup>31</sup>, and there is evidence to suggest that circulating DCs in breast cancer patients have reduced  
296 antigen presentation<sup>32</sup>. Therefore, we quantified costimulatory molecule expression on splenic DCs 2  
297 days post infection with *Lm*. We found that DCs from AT3 tumor-burdened animals expressed lower  
298 levels of key costimulatory molecules CD80 and CD86 and the activation marker CD83 when compared  
299 to healthy controls (Fig. 5d and Extended Data Fig. 9c). At a later time point coinciding with peak T cell  
300 responses (day 7 post-infection), DCs from tumor-burdened mice continued to exhibit signs of  
301 suboptimal activation, expressing lower levels of the adhesion molecule CD54 (ICAM-1) and PD-L1  
302 (Extended Data Fig. 9d). The latter result rules out the possibility that the PD-1/PD-L1 axis causes the  
303 impairment in T cell responses and indicates that alternative strategies are likely required to induce new  
304 systemic T cell activity. We therefore sought to pharmacologically boost APC activation as a plausible  
305 strategy for achieving this goal. Anti-CD40 treatment drives potent and systemic APC activation as  
306 shown by elevated CD86 and PD-L1 on splenic DCs (Fig. 5e and Extended Data Fig. 9e). In the context  
307 of infection, anti-CD40 treatment rescued the defect in CD8<sup>+</sup> T cell proliferation in tumor-burdened  
308 animals 7 days post infection with *Lm* (Fig. 5f). At this time point, we also observed significantly higher  
309 levels of activation markers CD54 and PD-L1 on DCs after treatment (Extended Fig. 9d), consistent with  
310 enhanced APC stimulation. In stark contrast, even high doses of IL-12p70 or treatment with anti-CTLA-4  
311 failed to rescue T cell proliferation (Fig. 5f and Extended Fig. 9f), suggesting that T cell targeted  
312 interventions alone are not sufficient. These experiments demonstrate that APCs fail to drive optimal new  
313 T cell responses in the context of tumor burden. Furthermore, these data suggest that effective  
314 immunotherapies should seek to boost APCs in combination with T cell focused treatments to fully  
315 enable *de novo* immune responses.

316

### 317 **Tumor resection reverses changes in systemic immune organization and responsiveness**

318 Given that defects in T cell proliferation and differentiation were reversed when T cells were  
319 removed from a tumor-burdened context, we asked whether tumor clearance was sufficient to revert all  
320 changes in systemic immune organization and function. We performed surgical resection of tumors at a

321 time when systemic changes were evident across sites and allowed mice to recover from surgery for an  
322 additional 14 days to mitigate immune confounders from wound healing. We carefully tracked both local  
323 recurrence and metastatic outgrowth by bioluminescent imaging. Impressively, we found that successful  
324 tumor resection reversed changes in systemic immunity in both the AT3 and 4T1 tumor models (Fig. 6a).  
325 Changes in both splenic immune cell frequencies and proliferative behavior became comparable to  
326 control animals across tissues (Fig. 6b-c, and Extended Fig. 10a-b). PCA of all major cell frequencies  
327 from both spleen and draining lymph node showed that resected animals closely resemble healthy  
328 controls along the first principal component (PC1: 43% of the variance for AT3, 57% for 4T1) (Fig. 6d).  
329 Similarly, the composition of T cell clusters in the spleen and lymph node was also largely reverted after  
330 resection (Fig. 6e). Finally, we asked whether the deficits in DC and T cell responses to infection were  
331 alleviated with tumor resection. We observed higher CD86 and PD-L1 expression on DCs at day 7 after  
332 *Lm* infection in resected mice, (Extended Fig. 10c-d) and both T cell proliferation and Granzyme B  
333 production after *Lm* infection were restored (Fig. 6f-g). Resected mice that had local or metastatic  
334 recurrence again showed deficits in DC activation and T cell responses (Extended Fig. 10c-e). Thus,  
335 changes in the systemic immune macroenvironment, unlike those of T cells in the TME, are highly  
336 dependent on the continual presence of the tumor and are dramatically reversible upon effective tumor  
337 clearance.

338

## 339 **Discussion**

340 This study constructs a comprehensive definition of the immune macroenvironment in cancer,  
341 capitalizing on recent technological advances to capture immune alterations across eight commonly used  
342 model systems, five sites of immune responses, and five time points in tumor progression, with 40  
343 proteins quantified on an average of two million individual cells per animal. We greatly expanded the  
344 understanding of tumor immunity by connecting local tumor interactions with corresponding perturbations  
345 in the systemic immune state. We show that immune organization is systemically disrupted across tumor  
346 types, and that these changes are distinct from the immune effects within the local TMEs. The systemic  
347 immune impacts were unique in each tumor type and accrued nonlinearly over time, suggesting unique

348 mechanisms of immune modulation and constant tumor-immune communication.

349 Immunotherapies vary in efficacy across cancer types, showing success in melanoma patients  
350 but only in a small subset of breast cancer patients<sup>33</sup>. Evidence of a strong pre-existing T cell response is  
351 associated with clinical benefit from currently available immunotherapies. In the remaining majority of  
352 cancer patients, it is likely that priming new immune responses will be required. Here, we show that  
353 tumor burden causes varying degrees of disruption in systemic immune state across tumor types, which  
354 is subtle in melanoma but dramatic in breast cancer. We demonstrate that severe disruptions in systemic  
355 immunity in breast cancer impair *de novo* immune responses even to highly immunogenic pathogens.  
356 Impaired new type 1 immune responses represent a fundamental, but previously unappreciated, obstacle  
357 for effective immunotherapy in patients who require priming of new T cell responses. Prior studies have  
358 connected systemic changes with relapse in breast cancer patients, showing altered immune gene  
359 signatures in uninvolved lymph nodes and blood of patients with metastatic versus non-metastatic  
360 disease<sup>34</sup>, and more recently that levels of circulating CD45RO- Foxp3<sup>high</sup> Tregs are predictive of future  
361 relapse<sup>35</sup>. Vast immune disruptions argue strongly for a combinatorial immunotherapeutic approach in  
362 this context. More work needs to be done to understand the extent of systemic immune alterations  
363 across cancer patients and tumor types, and how this may inform both the likelihood of disease  
364 dissemination and the optimal therapeutic strategy.

365 The ability of a tumor-burdened immune system to establish *de novo* immune responses is poorly  
366 defined<sup>36-38</sup>, yet it is clearly essential for successful anti-tumor immunity against less immunogenic  
367 tumors. Evidence exists that human cancer patients are more susceptible to opportunistic bacterial and  
368 viral infections and also mount less effective immune responses to vaccination when compared to  
369 healthy individuals<sup>39,40</sup>. How much of this difference is attributable to systemic impacts of tumor burden  
370 versus the effects of common cancer therapies has remained a matter of debate. We demonstrate that  
371 immunity is indeed functionally impaired as a consequence of tumor development. The coordination of  
372 adaptive immune responses to novel challenges that did not share antigens with the tumor was  
373 significantly dampened. This striking observation challenges the idea that T cell dysfunction in cancer is  
374 limited to tumor-specific T cells and driven largely by chronic antigen presentation. Instead, our data



375 indicate impairment in the initial coordination of a T cell response by APCs, ultimately impacting T cell  
376 proliferation and differentiation. It will be important to define the tumor-driven factors involved in failure of  
377 APCs to effectively support T cell responses across different tumor contexts.

378 Finally, these studies reveal remarkable plasticity in the systemic immune state. Systemic  
379 immune cells removed from the physiological context of the tumor responded normally to various  
380 challenges *in vitro* and *in vivo*. Surgical tumor resection was sufficient to revert the systemic immune  
381 landscape and function ability toward a healthy baseline. Tumor resection has previously been  
382 associated with a reduction in myeloid-derived suppressor cells<sup>19,41</sup>. Here, we extend these observations  
383 to characterize in depth the extent to which the systemic immune state is reversibly impacted, in both  
384 organization and in function. Influenced by the physiological immune context, immunotherapies will likely  
385 have drastically different consequences when applied pre- or post-operatively.

386 This study demonstrates that tumor burden drives immune programs that reach beyond local  
387 interactions. This rich data resource provides systemic immune context across all cell subsets and many  
388 tumor contexts, laying the foundation for detailed studies of specific tumor macroenvironments to match  
389 our detailed understanding of tumor microenvironments. Building a complete understanding of systems-  
390 level immunity in cancer should further our ability to drive effective and rationally designed antitumor  
391 immune responses in all cancer patients.

392

## 393 **METHODS**

### 394 **Animals**

395 All mice were housed in an American Association for the Accreditation of Laboratory Animal Care–accredited  
396 animal facility and maintained in specific pathogen-free conditions. Animal experiments were approved and  
397 conducted in accordance with Institutional Animal Care & Use Program protocol number AN157618. Wild-type  
398 female BALB/c, C57BL/6, and B6;129 F1 mice between 8-10 weeks old were purchased from The Jackson  
399 Laboratory and housed at our facility. 4T1 ( $1 \times 10^5$  cells / 100 $\mu$ l) or AT3 ( $5 \times 10^5$  cells / 100 $\mu$ l) breast cancer cells were  
400 transplanted into the fourth mammary fat pad. SB28 glioblastoma cells ( $1 \times 10^5$  cells / 2 $\mu$ l) were transplanted into the  
401 right cerebral hemisphere by stereotactic injection. MC38 colon cancer cells ( $1 \times 10^5$  cells / 100 $\mu$ l), B16-F10  
402 melanoma cancer cells ( $1 \times 10^5$  cells / 100 $\mu$ l), or LMP pancreatic cancer cells ( $2 \times 10^5$  cells / 100 $\mu$ l) were transplanted



403 into the subcutaneous region of the flank. Female MMTV-PyMT mice were bred at Stanford University. Tyr::CreER;  
404 Brat<sup>V600E/+</sup>; Pten<sup>lox/lox</sup> mice were purchased from Jackson Laboratory and housed at our facility. TCR Transgenic OT-  
405 I CD45.1 mice and heterozygous CD45.2/CD45.1 mice were bred at our facility. Animals were housed under  
406 standard SPF conditions with typical light/dark cycles and standard chow.

407

#### 408 **Cell Lines**

409 4T1 cells were gifted from Dr. Mary-Helen Barcellos-Hoff (UCSF). AT3 cells were gifted from Dr. Ross Levine  
410 (MSKCC). For *in vivo* experiments tracking tumor growth and recurrence after resection, we used 4T1 cells  
411 expressing mCherry-Luciferase and AT3 cells expressing GFP-Luciferase. SB28 cells, derived from a  
412 NRasV12;shp53;mPGDF transposon-induced glioma<sup>42</sup>, were gifted from Dr. Hideho Okada (UCSF). LMP cells,  
413 derived from the Kras<sup>G12D/+</sup>;LSL-Trp53<sup>R172H/+</sup>;Pdx-1-Cre model of pancreatic cancer<sup>43</sup>, were gifted from Dr. Edgar  
414 Engleman (Stanford University). MC38 cells and B16-F10 cells gifted from Dr. Jeffrey Bluestone (UCSF). 4T1,  
415 MC38, B16 and SB28 cells were cultured in RPMI-1640, and AT3 and LMP cells were cultured in DMEM, all  
416 supplemented with 10% FCS, 2 mM L-glutamine, 100 U/mL penicillin and 100 mg/mL penicillin/streptomycin.

417

#### 418 **Infectious Agents**

419 *Listeria monocytogenes* strain 10403s expressing OVA (*Lm*-OVA) was originally from Hao Shen<sup>44</sup> and kindly  
420 provided by Shomyseh Sanjabi (UCSF). *Lm*-OVA stocks frozen at -80 C were grown overnight at 37 C in BHI broth  
421 supplemented with 5 ug/ml Erythromycin. Then, overnight cultures were sub-cultured by diluting into fresh BHI  
422 broth supplemented with 5 ug/ml Erythromycin and grown for 4 hours. Bacteria CFU was then quantified by  
423 measuring optical density at 600 nm. Bacteria were then diluted to 5X10<sup>4</sup> CFU / 100μl in sterile PBS and 100 μl  
424 was injected per mouse i.v. via the retro-orbital vein.

425 Lymphocytic choriomeningitis virus (LCMV) was kindly provided by Dr. Jason Cyster (UCSF) and mice  
426 were infected with pre-titered and aliquoted stocks stored in PBS at -80C and diluted with sterile PBS. Mice were  
427 infected with 2x10<sup>5</sup> PFU by intraperitoneal injection.

428

#### 429 **Mass Cytometry Antibodies**

430 All mass cytometry antibodies and concentrations used for analysis can be found in Table S1. Primary conjugates  
431 of mass cytometry antibodies were prepared using the MaxPAR antibody conjugation kit (Fluidigm) according to the  
432 manufacturer's recommended protocol. Following labeling, antibodies were diluted in Candor PBS Antibody

433 Stabilization solution (Candor Bioscience GmbH, Wangen, Germany) supplemented with 0.02% NaN<sub>3</sub> to between  
434 0.1 and 0.3 mg/mL and stored long-term at 4°C. Each antibody clone and lot was titrated to optimal staining  
435 concentrations using primary murine samples.

436

#### 437 **Cell Preparation**

438 All tissue preparations were performed simultaneously from each individual mouse, as previously reported<sup>6</sup>. After  
439 euthanasia by CO<sub>2</sub> inhalation, peripheral blood was collected via the posterior vena cava prior to perfusion of the  
440 animal and transferred into sodium heparin-coated vacuum tubes prior to dilution in PBS with 5mM EDTA and 0.5%  
441 BSA (PBS/EDTA/BSA). Spleens and lymph nodes were homogenized in PBS/EDTA at 4°C. Bone marrow was  
442 flushed from femur and re-suspended in PBS/EDTA at 4°C. Tumors were finely minced and digested in RPMI-1640  
443 with 4 mg/ml collagenase IV, and 0.1 mg/ml DNase I. After digestion, re-suspended cells were quenched with  
444 PBS/EDTA at 4°C. All tissues were washed with PBS/EDTA and re-suspended 1:1 with PBS/EDTA and 100mM  
445 Cisplatin (Enzo Life Sciences, Farmingdale, NY) for 60 s before quenching 1:1 with PBS/EDTA/BSA to determine  
446 viability as previously described<sup>45</sup>. Cells were centrifuged at 500 g for 5 min at 4°C and re-suspended in  
447 PBS/EDTA/BSA at a density between 1-10\*10<sup>6</sup> cells/ml. Suspensions were fixed for 10 min at RT using 1.6% PFA  
448 and frozen at -80°C.

449

#### 450 **Mass-Tag Cellular Barcoding**

451 Mass-tag cellular barcoding was performed as previously described<sup>46</sup>. Briefly, 1\*10<sup>6</sup> cells from each animal were  
452 barcoded with distinct combinations of stable Pd isotopes in 0.02% saponin in PBS. Samples from any given tissue  
453 from each mouse per experiment group were barcoded together. Cells were washed once with cell staining media  
454 (PBS with 0.5% BSA and 0.02% NaN<sub>3</sub>), and once with 1X PBS, and pooled into a single FACS tube (BD  
455 Biosciences). After data collection, each condition was deconvoluted using a single-cell debarcoding algorithm<sup>46</sup>.

456

#### 457 **Mass Cytometry Staining and Measurement**

458 Cells were resuspended in cell staining media (PBS with 0.5% BSA and 0.02% NaN<sub>3</sub>) and metal-labeled antibodies  
459 against CD16/32 were added at 20 mg/ml for 5 min at RT on a shaker to block Fc receptors. Surface marker  
460 antibodies were then added, yielding 500 uL final reaction volumes and stained for 30 min at RT on a shaker.  
461 Following staining, cells were washed 2 times with cell staining media, then permeabilized with methanol for at 10  
462 min at 4°C. Cells were then washed twice in cell staining media to remove remaining methanol, and stained with

463 intracellular antibodies in 500 mL for 30 min at RT on a shaker. Cells were washed twice in cell staining media and  
464 then stained with 1mL of 1:4000 191/193lr DNA intercalator (Fluidigm) diluted in PBS with 1.6% PFA overnight.  
465 Cells were then washed once with cell staining media and then two times with double-deionized (dd)H<sub>2</sub>O. Care was  
466 taken to assure buffers preceding analysis were not contaminated with metals in the mass range above 100 Da.  
467 Mass cytometry samples were diluted in ddH<sub>2</sub>O containing bead standards (see below) to approximately 10<sup>6</sup> cells  
468 per mL and then analyzed on a CyTOF 2 mass cytometer (Fluidigm) equilibrated with ddH<sub>2</sub>O. We analyzed 1-5\*10<sup>5</sup>  
469 cells per animal, per tissue, per time point, consistent with generally accepted practices in the field.

470

#### 471 **Mass Cytometry Bead Standard Data Normalization**

472 Data normalization was performed as previously described<sup>6</sup>. Briefly, just before analysis, the stained and  
473 intercalated cell pellet was resuspended in freshly prepared ddH<sub>2</sub>O containing the bead standard at a  
474 concentration ranging between 1 and 2\*10<sup>4</sup> beads/ml. The mixture of beads and cells were filtered through a filter  
475 cap FACS tubes (BD Biosciences) before analysis. All mass cytometry files were normalized together using the  
476 mass cytometry data normalization algorithm<sup>47</sup>, which uses the intensity values of a sliding window of these bead  
477 standards to correct for instrument fluctuations over time and between samples.

478

#### 479 **Mass Cytometry Gating Strategy**

480 After normalization and debarcoding of files, singlets were gated by Event Length and DNA. Live cells were  
481 identified by Cisplatin negative cells. All positive and negative populations and antibody staining concentrations  
482 were determined by titration on positive and negative control cell populations.

483

#### 484 **Scaffold Map Generation**

485 Statistical scaffold maps were generated using the open source Statistical Scaffold R package available at  
486 [github.com/SpitzerLab/statisticalScaffold](https://github.com/SpitzerLab/statisticalScaffold) with modifications detailed below.

487 As previously described<sup>6</sup>, cells from each tissue for all animals were clustered together and then  
488 deconvolved into their respective samples. Cluster frequencies or the Boolean expression of specific proteins for  
489 each cluster were passed into the Significance Across Microarrays algorithm<sup>48,49</sup>, and the fold change results were  
490 reported (rather than the binary significance cutoff as originally implemented in Spitzer et al., 2017). Cluster  
491 frequencies were also correlated with the time from tumor inoculation using Spearman's rank-ordered correlation.  
492 All results were tabulated into the Scaffold map files for visualization through the graphical user interface, with

493 coloring modifications to graph the spectrum of fold change or correlation strength. The fold change was log<sub>2</sub>  
494 normalized and graphed with an upper and lower limit of a four-fold difference, unless otherwise indicated. Cluster  
495 frequencies were calculated as a percent of total live nucleated cells (excluding erythrocytes). The spleen data from  
496 the 4T1 model was used to spatialize the initial Scaffold map because all major, mature immune cell populations  
497 are present in that tissue.

498

### 499 **Cell Frequency Heat Map Generation**

500 Specified subsets, i.e. T cells and mononuclear phagocytes, were manually gated from each tissue for all animals  
501 and clustered together. Cluster frequencies were calculated as a percent of total live nucleated cells within that  
502 subset (excluding erythrocytes). T cells were identified as CD3<sup>+</sup>, CD11b<sup>-</sup>. Mononuclear phagocytes were defined as  
503 CD11b<sup>+</sup>, CD19<sup>-</sup>, CD3<sup>-</sup>, Ly6G<sup>-</sup>. Heatmaps of the resulting cluster frequencies were generated in R.

504

### 505 **Human Gene Expression Analysis**

506 Whole blood microarray data was generated by The Norwegian Women and Cancer (NOWAC) study and is  
507 deposited in the European Genome-Phenome Archive under accession number EGAS00001001804 as previously  
508 reported<sup>50</sup>. Principal component analysis of centered and scaled data was performed in R using the prcomp  
509 function. xCell cell type enrichment analysis was performed in R using the xCell package  
510 (<https://github.com/dviraran/xCell>) using a customized list of cell populations known to exist in peripheral whole  
511 blood (B-cells, Basophils, CD4<sup>+</sup> memory T-cells, CD4<sup>+</sup> naive T-cells, CD4<sup>+</sup> T-cells, CD4<sup>+</sup> Tcm, CD4<sup>+</sup> Tem, CD8<sup>+</sup>  
512 naive T-cells, CD8<sup>+</sup> T-cells, CD8<sup>+</sup> Tcm, CD8<sup>+</sup> Tem, cDC, Class-switched memory B-cells, Eosinophils,  
513 Erythrocytes, Megakaryocytes, Memory B-cells, Monocytes, naive B-cells, Neutrophils, NK cells, NKT, pDC,  
514 Plasma cells, Platelets, Tgd cells, Th1 cells, Th2 cells, Tregs).

515

### 516 ***In vitro* CD8 T cell Differentiation and cytokine production**

517 Mice bearing 21-day AT3 tumors were euthanized and their spleens harvested and dissociated. CD8 T cells were  
518 enriched using the EasySep Streptavidin Negative Selection Kit with the following biotinylated markers: CD11b,  
519 MHCII, CD11c, Gr1, B220, CD4, CD44, and Ter119. Isolated CD8 T cells were then stimulated with plate-bound  
520 CD3 and suspended in CD28 containing T cell media for 3 days. The cells were then removed from CD3/CD28  
521 stimulation and rested for 1 day. Cells were then restimulated with PMA & Ionomycin or left unstimulated for 4  
522 hours with Brefeldin A and analyzed by flow cytometry.

523

## 524 **Adoptive T Cell Transfer**

525 For OT1 and polyclonal adoptive transfers, CD8 T cells were isolated from spleens of CD45.1 OT1 TCR transgenic  
526 or CD45.1/CD45.2 heterozygote wildtype or CD45.1 BoyJ mice by enrichment with EasySep Streptavidin Negative  
527 Selection Kit with the following biotinylated markers: CD11b, MHCII, CD11c, Gr1, B220, CD4, and Ter119. Cells  
528 were stained with CFSE or Cell Trace Violet and  $1 \times 10^5$  cells were then adoptively transferred into each recipient  
529 mouse via the retroorbital vein.

530

## 531 **Quantifying Bacterial Burden**

532 To quantify bacterial burden, spleens were harvested and dissociated. Cells from each mouse were lysed in 0.5%  
533 TritonX 100 in PBS and cells were serially diluted in duplicate and aliquots were then added to BHI agar and  
534 incubated overnight at 37C. Colonies grown were then counted to quantify bacterial CFU present.

535

## 536 **Treatments**

537 All *in vivo* antibody treatments were given i.p. starting on day 0 of *Lm*-Ova infection: 200  $\mu$ g of agonistic CD40  
538 (FGK4.5, BioXCell) on day 0, 225  $\mu$ g of recombinant IL-12p70 (BioLegend) daily, and 200  $\mu$ g of antagonistic CTLA-  
539 4 (9H10, BioXCell) on day 0 and day 3.

540

## 541 **Tumor Resection**

542 Mice bearing 14-day 4T1 tumors or 16 to 21-day AT3 tumors (between 350-550mm<sup>3</sup>) were anesthetized by  
543 intraperitoneal (i.p) injection with a mixture of ketamine and xylazine, and titrated to effect with isoflurane from a  
544 precision vaporizer. The surgical site was shaved and sterilized with 70% ethanol and 10% povidone iodine. An  
545 incision was made subcutaneously at the anterior midline and along the flank of the side with the tumor, using  
546 surgical scissors, to reveal the inguinal mammary tumor. The tumor was teased away using forceps and the  
547 surgical wound closed with wound clips. Wound clips were removed after 7 days. 10-20% of resected mice had  
548 tumor recurrence due to incomplete removal of primary tumors or outgrowth of micro-metastases. These mice were  
549 excluded from the experiments to which they were initially assigned.

550

## 551 **Flow Cytometry**

552 Cells were stained for viability with Zombie-NIR stain. Cell surface staining was performed in cell staining media

553 (PBS with 0.5% BSA and 0.02% NaN<sub>3</sub>) for 15 minutes at room temperature. Intracellular staining was performed  
554 after fixing cells with BioLegend FluoroFix Buffer and permeabilizing cells with Biolegend's Intracellular Staining  
555 Perm Wash Buffer. The following anti-mouse antibodies were used: (PE-Dazzle594) – CD3 (clone 17A2),  
556 (PacificBlue) – CD4 (clone RM4-5), (BV786) – CD8 (clone 53-6.7), (APC-Cy7) – CD45 (clone 30-F11), (APC) –  
557 CD38 (clone 90), (PE) – CD101 (clone Moushi101) , (PD1) – PE-Cy7 (clone 29F.1A12), (BV421) – TCRb (clone  
558 H57-597), (PE) – IFN $\gamma$  (clone XMG1.2), (BV711) – IL2 (clone JES6-5H4), (FITC) – TNF $\alpha$  (clone MP6-XT22),  
559 (BV650) – CD8 (clone 53-6.7), (PE) – CD45.1 (clone A20). All antibodies were purchased from Biolegend, Inc., BD  
560 Biosciences, or Thermo Fisher Scientific. Stained cells were analyzed with a CytoFLEX flow cytometer (Beckman  
561 Coulter) or an LSR II flow cytometer (BD Biosciences).

562 Singlets were gated by FSC-A and FSC-W, as well as by SSC-A and SSC-W. All positive and negative  
563 populations were determined by staining on positive and negative control populations.

564

## 565 **QUANTIFICATION AND STATISTICAL ANALYSIS**

566 Comparison of cell frequencies and protein expression in Statistical Scaffold was performed using Significance  
567 Analysis of Micro-arrays as described above and in Bair and Tibshirani, 2004 and Bruggner et al., 2014. Analysis of  
568 principle components for human gene expression was performed using two-tailed Wilcoxon rank-Sum test in R. All  
569 comparisons over 4T1 tumor growth were performed by One-way ANOVA with Tukey correction in Prism. All other  
570 comparisons after infection, treatment, or resection were made using two-tailed t tests in Prism. All tests with  $q <$   
571 0.05 were considered statistically significant. Unless otherwise stated,  $n = 3$  to 6 independent mice for each  
572 experimental condition.

## 573 **DATA AND SOFTWARE AVAILABILITY**

574 The updated Statistical Scaffold package and all mass cytometry data will be made publicly available concurrent  
575 with publication of the manuscript.

576

## 577 **ACKNOWLEDGMENTS**

578 We thank the UCSF Flow Cytometry Core and Stanley Tamaki for CyTOF maintenance, Drs. Mary-Helen  
579 Barcellos-Hoff, Ross Levine, Hideho Okada, Edgar Engleman and Jeffrey Bluestone for cell lines,  
580 transgenic mice and reagents, and Iliana Tenvooren and Diana Marquez for assistance in animal work.  
581 This work was supported by NIH grants DP5OD023056 and P50CA097257 (UCSF Brain Tumor SPORE

582 Developmental Research Program) and investigator funding from the Parker Institute for Cancer  
583 Immunotherapy to M.H.S., and by NIH grant S10OD018040, which enabled procurement of the mass  
584 cytometer used in this study.

585

586 M.H.S. receives research funding from Roche/Genentech and Valitor Inc. and has been a paid  
587 consultant for Five Prime Therapeutics and Ono Pharmaceutical.

588

### 589 **AUTHOR CONTRIBUTIONS**

590 Conceptualization, B.M.A, K.J.H., Y.C., and M.H.S.; Experimental Methodology, B.M.A, K.J.H., C.E.B.,  
591 A.V., R.B., Y.C., and M.H.S.; Computational Methodology, B.M.A, and M.H.S.; Investigation, all authors;  
592 Writing – Original Draft, B.M.A.; Writing – Review & Editing, all authors; Funding Acquisition, M.H.S.;  
593 Supervision, M.H.S.

594

595



## 596 REFERENCES

- 597 1. Azizi, E. *et al.* Single-Cell Map of Diverse Immune Phenotypes in the Breast Tumor  
598 Microenvironment. *Cell* **174**, 1293–1308 (2018).
- 599 2. Joyce, J. A. & Fearon, D. T. T cell exclusion, immune privilege, and the tumor microenvironment.  
600 *Science*. **348**, 74–80 (2015).
- 601 3. Wagner, J. *et al.* A Single-Cell Atlas of the Tumor and Immune Ecosystem of Human Breast  
602 Cancer. *Cell* **177**, 1–16 (2019).
- 603 4. Tsujikawa, T. *et al.* Quantitative Multiplex Immunohistochemistry Reveals Myeloid-Inflamed  
604 Tumor-Immune Complexity Associated with Poor Prognosis. *Cell Rep.* **19**, 203–217 (2017).
- 605 5. Philip, M. *et al.* Chromatin states define tumour-specific T cell dysfunction and reprogramming.  
606 *Nature* **545**, 452–456 (2017).
- 607 6. Spitzer, M. H. *et al.* Systemic Immunity Is Required for Effective Cancer Immunotherapy. *Cell* **168**,  
608 487–502 (2017).
- 609 7. Fransen, M. F. & Van Hall, T. Tumor-draining lymph nodes are pivotal in PD-1/PD-L1 checkpoint  
610 therapy. *JCI Insight* **3**, e124507 (2018).
- 611 8. Tang, H. *et al.* PD-L1 on host cells is essential for PD-L1 blockade-mediated tumor regression. *J*  
612 *Clin Invest* **128**, 580–588 (2018).
- 613 9. Chamoto, K. *et al.* Mitochondrial activation chemicals synergize with surface receptor PD-1  
614 blockade for T cell-dependent antitumor activity. *PNAS* **114**, E761–E770 (2017).
- 615 10. Mathios, D. *et al.* Anti – PD-1 antitumor immunity is enhanced by local and abrogated by systemic  
616 chemotherapy in GBM. *Sci. Transl. Med.* **8**, 1–12 (2016).
- 617 11. Yost, K. E. *et al.* Clonal replacement of tumor-specific T cells following PD-1 blockade. *Nat. Med.*  
618 **25**, 1251–1259 (2019).
- 619 12. McAllister, S. S. & Weinberg, R. A. The tumour-induced systemic environment as a critical  
620 regulator of cancer progression and metastasis. *Nat. Cell Biol.* **16**, 717–727 (2014).
- 621 13. Zhang, S. *et al.* The Role of Myeloid-Derived Suppressor Cells in Patients with Solid Tumors: A  
622 Meta-Analysis. *PLoS One* **11**, e0164514 (2016).
- 623 14. Casbon, A.-J. *et al.* Invasive breast cancer reprograms early myeloid differentiation in the bone  
624 marrow to generate immunosuppressive neutrophils. *Proc. Natl. Acad. Sci. U. S. A.* **112**, E566-75  
625 (2015).
- 626 15. Meyer, M. A. *et al.* Breast and pancreatic cancer interrupt IRF8-dependent dendritic cell  
627 development to overcome immune surveillance. *Nat. Commun.* **9**, 1–19 (2018).
- 628 16. Barnstorf, I. *et al.* Chronic virus infection compromises memory bystander T cell function in an IL-  
629 6/ STAT1-dependent manner. *J. Exp. Med* **216**, 571–586 (2019).
- 630 17. Snell, L. M. *et al.* CD8 + T Cell Priming in Established Chronic Viral Infection Preferentially Directs  
631 Differentiation of Memory-like Cells for Sustained Immunity. *Immunity* **49**, (2018).
- 632 18. Osborne, L. C. *et al.* Virus-helminth coinfection reveals a microbiota-independent mechanism of



- 633 immunomodulation. *Science*. **345**, 578–582 (2014).
- 634 19. Ghochikyan, A. *et al.* Primary 4T1 tumor resection provides critical “window of opportunity” for  
635 immunotherapy. *Clin Exp Metastasis* **31**, 185–198 (2014).
- 636 20. Schietinger, A. *et al.* Tumor-Specific T Cell Dysfunction Is a Dynamic Antigen-Driven  
637 Differentiation Program Initiated Early during Tumorigenesis. *Immunity* **45**, 389–401 (2016).
- 638 21. Anderson, K. G., Stromnes, I. M. & Greenberg, P. D. Cancer Cell Perspective Obstacles Posed by  
639 the Tumor Microenvironment to T cell Activity: A Case for Synergistic Therapies. *Cancer Cell* **31**,  
640 311–325 (2017).
- 641 22. Anz, D. *et al.* CD103 is a hallmark of tumor-infiltrating regulatory T cells. *Int. J. Cancer* **129**, 2417–  
642 2426 (2011).
- 643 23. Ross, E. A. *et al.* CD31 is required on CD4 + T cells to promote T cell survival during Salmonella  
644 infection. *J. Immunol.* **187**, 1553–1565 (2011).
- 645 24. Hanninen, A., Maksimow, M., Alam, C., Morgan, D. J. & Jalkanen, S. Ly6C supports preferential  
646 homing of central memory CD81 T cells into lymph nodes. *Eur. J. Immunol.* **41**, 634–644 (2011).
- 647 25. Fourcade, J. *et al.* Upregulation of Tim-3 and PD-1 expression is associated with tumor antigen–  
648 specific CD8+ T cell dysfunction in melanoma patients. *J. Exp. Med.* **207**, 2175–2186 (2010).
- 649 26. Mita, Y. *et al.* Crucial role of CD69 in anti-tumor immunity through regulating the exhaustion of  
650 tumor-infiltrating T cells. *Int. Immunol.* **30**, 559–567 (2018).
- 651 27. Sun, C., Mezzadra, R. & Schumacher, T. N. Regulation and Function of the PD-L1 Checkpoint.  
652 *Immunity* **48**, 434–452 (2018).
- 653 28. Bianchini, M. *et al.* PD-L1 expression on nonclassical monocytes reveals their origin and  
654 immunoregulatory function. *Sci. Immunol.* **4**, eaar3054 (2019).
- 655 29. Busch, D. H., Pilip, I. M., Vijh, S. & Pamer, E. G. Coordinate regulation of complex T cell  
656 populations responding to bacterial infection. *Immunity* **8**, 353–362 (1998).
- 657 30. Kaech, S. M. & Ahmed, R. Memory CD8 + T cell differentiation: initial antigen encounter triggers a  
658 developmental program in naïve cells. *Nat. Immunol.* **2**, 415–422 (2001).
- 659 31. Jung, S. *et al.* In vivo depletion of CD11c+ dendritic cells abrogates priming of CD8+ T cells by  
660 exogenous cell-associated antigens. *Immunity* **17**, 211–220 (2002).
- 661 32. Gabrilovich, D. I., Corak, J., Ciernik, I. F., Kavanaugh, D. & Carbone, D. P. Decreased antigen  
662 presentation by dendritic cells in patients with breast cancer. *Clin. Cancer Res.* **3**, 483–490 (1997).
- 663 33. Schmid, P. *et al.* Atezolizumab and Nab-Paclitaxel in Advanced Triple-Negative Breast Cancer. *N.*  
664 *Engl. J. Med.* **379**, 2108–2121 (2018).
- 665 34. Zuckerman, N. S. *et al.* Altered local and systemic immune profiles underlie lymph node  
666 metastasis in breast cancer patients. *Int. J. Cancer* **132**, 2537–2547 (2012).
- 667 35. Wang, L. *et al.* Connecting blood and intratumoral Treg cell activity in predicting future relapse in  
668 breast cancer. *Nat. Immunol.* **20**, 1220–1230 (2019).
- 669 36. Mittal, R., Wagener, M., Breed, E. R., Liang, Z. & Yoseph, B. P. Phenotypic T Cell Exhaustion in a

- 670 Murine Model of Bacterial Infection in the Setting of Pre-Existing Malignancy. *PLoS One* **9**, 93523  
671 (2014).
- 672 37. Xie, J. *et al.* Pre-existing malignancy results in increased prevalence of distinct populations of  
673 CD4+ T cells during sepsis. *PLoS One* **13**, e0191065 (2018).
- 674 38. Russ, A. J. *et al.* Melanoma-induced suppression of tumor antigen-specific T cell expansion is  
675 comparable to suppression of global T cell expansion. *Cell. Immunol.* **271**, 104–109 (2011).
- 676 39. Klastersky, J. & Aoun, M. Opportunistic infections in patients with cancer. *Ann. Oncol.* **15**, iv329–  
677 iv335 (2004).
- 678 40. Baluch, A. & Pasikhova, Y. Influenza Vaccination in Oncology Patients. *Curr Infect Dis Rep* **15**,  
679 486–490 (2013).
- 680 41. Danna, E. A. *et al.* Surgical Removal of Primary Tumor Reverses Tumor-Induced  
681 Immunosuppression Despite the Presence of Metastatic Disease. *Cancer Res.* **64**, 2205–2211  
682 (2004).
- 683 42. Kosaka, A., Ohkuri, T., Program, B. T. & Okada, H. Combination of an agonistic anti-CD40  
684 monoclonal antibody and the COX-2 inhibitor celecoxib induces anti-glioma effects by promotion  
685 of type-1 immunity in myeloid cells and T-cells. *Cancer Immunol Immunother* **63**, 847–857 (2014).
- 686 43. Tseng, W. W. *et al.* Cancer Therapy: Preclinical Development of an Orthotopic Model of Invasive  
687 Pancreatic Cancer in an Immunocompetent Murine Host. *Clin. Cancer Res.* **16**, 3684–3695  
688 (2010).
- 689 44. Kathryn E. Foulds, Lauren A. Zenewicz, Devon J. Shedlock, J. J. & Amy E. Troy, and H. S.  
690 Cutting Edge: CD4 and CD8 T Cells Are Intrinsically Different in Their Proliferative Responses. *J*  
691 *Immunol* **168**, 1528–1532 (2002).
- 692 45. Spitzer, M. H. *et al.* An interactive reference framework for modeling a dynamic immune system.  
693 *Immunology* **349**, 1259425.1-1259425.11 (2015).
- 694 46. Zunder, E. R. *et al.* Palladium-based Mass-Tag Cell Barcoding with a Doublet-Filtering Scheme  
695 and Single Cell Deconvolution Algorithm. *Nat. Protoc.* **10**, 316–333 (2015).
- 696 47. Finck, R. *et al.* Normalization of mass cytometry data with bead standards. *Cytom. Part A* **83 A**,  
697 483–494 (2013).
- 698 48. Bair, E. & Tibshirani, R. Semi-Supervised Methods to Predict Patient Survival from Gene  
699 Expression Data. *PLoS Biol.* **2**, 0511–0522 (2004).
- 700 49. Robert V. Bruggner, Bernd Bodenmiller, D. L. D. & Robert J. Tibshirani, and G. P. N. Automated  
701 identification of stratifying signatures in cellular subpopulations. *PNAS* **26**, E2770–E2777 (2014).
- 702 50. Dumeaux, V. *et al.* Interactions between the tumor and the blood systemic response of breast  
703 cancer patients. *PLoS Comput. Biol.* **13**, e1005680 (2017).

704

## 705 MAIN FIGURE LEGENDS

### 706 Fig. 1: The systemic immune landscape is remodeled across tumor models.

707 **a**, Composition of the tumor immune infiltrate across mouse tumor models at late stage tumor burden, identified  
708 manually. **b-c**, Principal component analysis (PCA) of the tumor infiltrating immune cell frequencies (**b**), and the  
709 log<sub>2</sub> fold change of immune cell frequencies for the tumor draining lymph node, bone marrow, blood, and spleen (**c**)  
710 identified manually. **d**, Scaffold maps of spleen immune cell frequencies in breast tumor models (4T1, AT3, and  
711 MMTV-PyMT). Black nodes represent canonical cell populations identified manually. Other nodes reflect  
712 unsupervised clustering of leukocytes (see Methods). Red denotes populations significantly higher in frequency in  
713 tumor-burdened animals compared to healthy; blue denotes significantly lower frequency. For significant nodes,  
714 degree coloring reflects log<sub>2</sub> fold change. **e-f**, PCA (**e**) and significant immune changes by cellular enrichment  
715 analysis (**f**) from human whole blood gene expression, comparing breast cancer patients (n = 173) and matched  
716 controls (n = 281).

717

### 718 Fig. 2: The systemic immune landscape is remodeled progressively with tumor development.

719 **a-b**, Scaffold maps of 4T1 tumor (**a**) and spleen (**b**) cell frequencies colored by significant Spearman correlation  
720 with time (across day 0, 7, 14, 21 and 35). Green denotes positive correlation, and brown denotes negative  
721 correlation. **c**, PCA of immune cell frequencies from each immune tissue over 4T1 breast tumor growth. Vectors  
722 designate progression from control day 0 (first point) to day 7, 14, 21, and 35 (last point, arrowhead). **d**, Curves of  
723 mean cell frequencies across time from immune cell types contributing to **c**, colored by tissue corresponding with **c**.

724

### 725 Fig. 3: Tumor burden progressively changes the systemic T cell composition.

726 **a-d**, CD3<sup>+</sup> CD11b<sup>-</sup> leukocytes from all tissues clustered together from healthy and 4T1 tumor-burdened animals at  
727 progressive time points. **a**, Scaffold maps of the T cell cluster frequencies in the spleen at each disease stage,  
728 colored by fold change in frequency compared to the previous time point. **b**, Heatmap of the protein expression  
729 defining each T cell cluster, column normalized to each protein's maximum positive expression. **c**, Heatmap of each  
730 T cell cluster frequency, by row, in each site and across the individual 3-4 animals per time point. **d**, Stacked bar  
731 plot of the log<sub>2</sub> fold change in cluster frequency between early (day 7) and late (day 35) disease stage, colored by  
732 tissue. **e-j**, Representative scatter plots of key proteins defining T cell clusters that change in frequency in the  
733 designated tissues between early and late disease stage for Tregs (**e**), CD4 T cells (**f-h**), and CD8 T cells (**i-j**). **k**,  
734 Representative scatter plots and quantification of CD101<sup>+</sup> CD38<sup>+</sup> dysfunctional CD8 T cells in the spleen and

735 tumor of health or day 21 tumor-burdened animals.

736

737 **Fig. 4: Tumor burden leads to impaired T cell responses to secondary infection.**

738 **a-b**, Fold change in body weight after *Listeria monocytogenes* (*Lm*) infection (**a**), and quantification of *Lm* bacterial  
739 burden (**b**) in control and AT3 tumor-burdened animals. **c**, Scaffold maps of CD8 T cell frequencies in the spleen in  
740 AT3 tumor-burdened mice after 7 days of *Lm* infection, colored by fold change in frequency compared to infected  
741 control mice. **d-e**, Quantification and representative scatter plots of splenic CD8<sup>+</sup> T cell proliferation (**d**) and  
742 Granzyme B production (**e**) in response to LCMV Armstrong or *Lm* in healthy or AT3 tumor-burdened animals.

743

744 **Fig. 5: Tumor burden attenuates dendritic cell activation during secondary infection.**

745 **a**, Proliferation dyes on OT-I T cells harvested from control or tumor-burdened animals, adoptively transferred into  
746 control recipients, and analyzed at 72, 96, and 144 hours post infection with *Lm*-Ova. Quantification shown for 96  
747 hours. Dyes diluted out by 144 hours. **b**, Absolute cell count of adoptively transferred OT-I T cells and their median  
748 signal intensity of T-bet and PD-1 at day 6 of *Lm*-OVA infection. **c**, Absolute cell count of competitively transferred  
749 polyclonal CD8 T cells from congenic (CD45.1<sup>+</sup> AT3 tumor-burdened or CD45.1<sup>+</sup>CD45.2<sup>+</sup> control) donors into  
750 CD45.2 control or AT3 tumor-burdened recipients, after 7 days of *Lm* infection. **d**, Median signal intensity of  
751 costimulatory proteins CD80 and CD86, and activation marker CD83 on splenic classical dendritic cells (cDCs)  
752 from healthy or AT3 tumor-burdened (day 28) mice, at day 2 of *Lm*-OVA infection. **e**, Median signal intensity of  
753 CD86 on splenic cDCs from untreated or CD40 treated AT3 tumor-burdened (day 21) mice. **f**, Quantification of  
754 splenic CD8<sup>+</sup> T cell proliferation in response to *Lm*-OVA in healthy versus untreated, IL-12p70 treated, or CD40  
755 treated AT3 tumor-burdened animals at day 7 of infection.  $p^* < 0.05$ , two-tailed t-test.

756

757 **Fig. 6: Tumor resection completely resets the systemic immune landscape.**

758 **a**, Heatmap of immune cell frequencies from tumor-burdened, T, or resected, R mice in peripheral tissues, shown  
759 as log<sub>2</sub> fold change from control. **b-c**, Scaffold maps of spleen immune cell frequencies (**c**) and proliferation by  
760 Ki67 expression (**c**) in AT3 resected mice compared to healthy control. Insets show resected compared to tumor-  
761 burdened mice. **d-e**, PCA of all immune cell frequencies (**d**) or T cell cluster frequencies (**e**) from the spleen and  
762 tumor draining lymph node of control, tumor-burdened, or resected mice. **f-g**, Quantification and representative  
763 scatter plots of splenic CD8<sup>+</sup> T cell proliferation (**f**) and Granzyme B production (**g**) in response to *Lm* infection in  
764 healthy, AT3 tumor-burdened, or resected mice (n = 1 to 13 per group, across 3 independent experiments).

765  $p^* < 0.05$ , two-tailed t-test.

## 766 **EXTENDED DATA FIGURE LEGENDS**

### 767 ***Extended Data Fig. 1: Main Mass Cytometry Gating Scheme.***

768 **a**, Main gating strategy for identifying major immune cell populations from mass cytometry datasets.

769

### 770 ***Extended Data Fig. 2: Systemic immunity is distinctly remodeled across tumor models.***

771 **a**, Relative abundance of total leukocytes infiltrating the TME across eight tumor models. **b-f**, Scaffold maps of  
772 spleen cell frequencies across five distinct tumor models, SB28 glioblastoma (**b**), MC38 colorectal (**c**), LMP  
773 pancreatic (**d**), B16 melanoma (**e**), and Braf-PTEN melanoma (**f**), comparing late stage tumor burden to their  
774 respective health littermate controls.

775

### 776 ***Extended Data Fig. 3: Systemic immunity is distinctly remodeled over tumor development.***

777 **a**, Pearson correlation between tumor mass and absolute number of infiltrating leukocytes in 4T1 breast tumors. **b**,  
778 Spleen immune absolute cell counts, adjusted absolute cell counts per mg of tissue, and unadjusted immune  
779 frequencies at each time point for neutrophils, B cells and T cells of the 4T1 breast tumor model. **c**, PCA of relative  
780 immune cell frequencies from each major immune tissue over time in the MMTV-PyMT breast tumor model.  
781 Vectors designate progression from control (first point) to 25 mm<sup>2</sup>, 50mm<sup>2</sup>, 125mm<sup>2</sup>, and 400mm<sup>2</sup> (last point,  
782 arrowhead). **d**, Scaffold maps of immune cell frequencies in the spleen at each time point of 4T1 tumor burden,  
783 colored by log<sub>2</sub> fold change in frequency compared to the previous time point.

784

### 785 ***Extended Data Fig. 4: Immunity is distinctly remodeled by compartment over tumor development.***

786 **a-d**, Scaffold maps of immune cell frequencies over 4T1 tumor progression in the tumor draining lymph node (**a**)  
787 blood (**b**), bone marrow (**c**), and tumor (**d**), colored by fold change relative to the previous time point.

788

### 789 ***Extended Data Fig. 5: Tumor growth shifts the systemic T cell composition across models.***

790 **a-b**, PCA of T cell cluster frequencies across lymphoid tissues over tumor development for the 4T1 (**a**) and MMTV-  
791 PyMT (**b**) breast tumor models. Vectors designate directional progression from control (first point) to late stage  
792 disease (last point, arrowhead). In **a**, tumor time points include day 7, 14, 21, and 35 after 4T1 cancer cell  
793 transplant. In **b**, tumor time points include tumor sizes of 25 mm<sup>2</sup>, 50 mm<sup>2</sup>, 125 mm<sup>2</sup>, and 400 mm<sup>2</sup>. **c-e**, CD3+  
794 CD11b- leukocytes from all tissues clustered together from healthy and MMTV-PyMT tumor-burdened animals at

795 progressive tumor sizes. **c**, Heatmap of each T cell cluster frequency, by row, in each site and across the individual  
796 2-3 animals per time point. **d**, Stacked bar plot of the log<sub>2</sub> fold change in cluster frequency between early (25 mm<sup>2</sup>)  
797 and late (400 mm<sup>2</sup>) disease time points, colored by tissue. **e**, Heatmap of the protein expression defining each T  
798 cell cluster, column normalized to each protein's maximum positive expression. **f-h**, Representative scatter plots of  
799 key proteins that define T cell clusters changing in frequency in the designated site between early and late disease  
800 stage for CD8 T cells (**f**), Tregs (**g**), and CD4 T Cells (**h**).

801

802 **Extended Data Fig. 6: Tumor growth shifts the systemic mononuclear phagocyte composition.**

803 **a**, CD3- CD19- leukocytes from all tissues clustered together from healthy and 4T1 tumor-burdened animals at  
804 progressive time points. *Left*, stacked bar plot of the log<sub>2</sub> fold change in cluster frequency between early (day 7)  
805 and late (day 35) times points, colored by tissue. *Right*, heatmap of the protein expression defining each cluster,  
806 column normalized to each protein's maximum positive expression. **b**, Curves of the mean cell frequencies over  
807 time in the 4T1 breast tumor model from designated mononuclear phagocyte cell types, colored by tissue. **c**, PCA  
808 of the mononuclear phagocyte cell frequencies from each tissue over time in the 4T1 breast tumor model. Vectors  
809 designate progression from control (first point) to day 7, 14, 21, and 35 (last point, arrowhead). Coloring of tissues  
810 for a-c corresponds to labels in c.

811

812 **Extended Data Fig. 7: PD-1 and PD-L1 expression is dynamic over tumor growth.**

813 **a**, Distribution of PD-1 and PD-L1 signal intensities on tumor infiltrating leukocytes over time in the 4T1 or AT3  
814 breast tumor models. Coloring of time points for a-d corresponds to legend in a. **b**, Percent of total infiltrating  
815 leukocytes (*left of dashed line*) or CD45-, non-endothelial cells (*right of dashed line*) with high PD-1 or PD-L1  
816 expression in the 4T1 or AT3 tumor models. **c**, Percent of leukocytes with high PD-1 or PD-L1 expression over time  
817 and across tissues, 4T1 model. **d**, Pearson correlation between median PD-L1 signal intensity on blood versus  
818 tumor infiltrating leukocytes, 4T1 model. **e**, Percent of each major immune cell subset expressing high PD-1 or PD-  
819 L1 in the tumor, blood, and spleen, identified manually. Cell subsets below 0.2% of total leukocytes were not  
820 included, X. Bars ordered by time point, beginning at healthy control. Double positive PD-1/PD-L1 expression was  
821 rare and not illustrated.  $p^* < 0.05$ , One-Way ANOVA, with Tukey correction versus control tissue or healthy  
822 mammary fat pad (blue in b-c, fill corresponding to bar color in e), or versus day 7 (green in b-c).

823

824 **Extended Data Fig. 8: Tumor burden induces tissue-specific changes in immune cell cycling.**



825 **a-b**, Log2 fold change in bulk Ki67 expressing leukocytes in each tissue tissues for 4T1, AT3 and MMTV breast  
826 tumors (**a**), and over 4T1 tumor progression (**b**).  $p^* < 0.05$ , One-Way ANOVA, with Tukey correction versus control.  
827 **c-d**, Statistical Scaffold maps of Ki67 expression in immune cells of the tumor draining lymph node comparing  
828 control to day 21 (**c**) and the Spleen over time (**d**) in 4T1 tumor burdened animals. **e**, Percent of increasing clusters  
829 (red, total of 56) or decreasing clusters (blue, total of 90) that have corresponding changes in cell cycle markers  
830 Ki67 and cleaved Caspase-3.

831

832 **Extended Data Fig. 9: Tumor driven deficits in T cell responses are cell-extrinsic.**

833 **a**, Expression of inflammatory cytokines, INF $\gamma$ , IL-2, and TNF $\alpha$  in splenic CD8 T Cells isolated from control or AT3  
834 tumor-burdened mice after *in vitro* differentiation with CD3, CD28 and IL-2, and re-stimulation with BrefeldinA and  
835 PMA Ionomycin. **b**, Scatter plots of CD11b and Ly6G showing expected neutrophilia in OT-I TCR transgenic mice  
836 with AT3 tumor burden. **c**, Histograms of CD80, CD86, and CD83 signal intensity on cDCs from healthy or AT3  
837 tumor-burdened mice at day 2 of *Lm*-OVA infection. **d**, Median signal intensity of PD-L1 and CD54 activation  
838 markers on splenic cDCs from healthy or AT3 tumor-burdened mice compared to IL-12p70 or CD40 treatment at  
839 day 7 of *Lm*-OVA infection. **e**, Median signal intensity of PD-L1 on splenic cDCs from untreated or CD40 treated  
840 AT3 tumor-burdened (day 21) mice. **f**, Quantification of splenic CD8<sup>+</sup> T cell proliferation in healthy, untreated or  
841 CTLA-4 treated AT3 tumor-burdened animals in response to 7 days of *Lm*-OVA infection.  $p^* < 0.05$ , two-tailed t-test.

842

843 **Extended Data Fig. 10: Tumor resection resets systemic immune organization and function.**

844 **a-b**, Statistical scaffold maps of spleen immune cell frequencies (**a**) and proliferation by Ki67 expression (**b**) in 4T1  
845 resected mice compared to health control. Insets show resected mice compared to tumor-burdened mice. **c-d**,  
846 Median signal intensity of CD86 (**c**) and PD-L1 (**d**) on splenic cDCs from healthy, AT3 tumor-burdened, resected, or  
847 resected mice with recurrence at day 7 of *Lm*-OVA infection.  $p^* < 0.05$ , two-tailed t-test. **e**, Quantification of splenic  
848 CD8<sup>+</sup> T cell proliferation and Granzyme B production in response to *Lm*-OVA in healthy versus resected mice with  
849 local or metastatic recurrence.

**Fig. 1: The systemic immune landscape is remodeled across tumor models.**

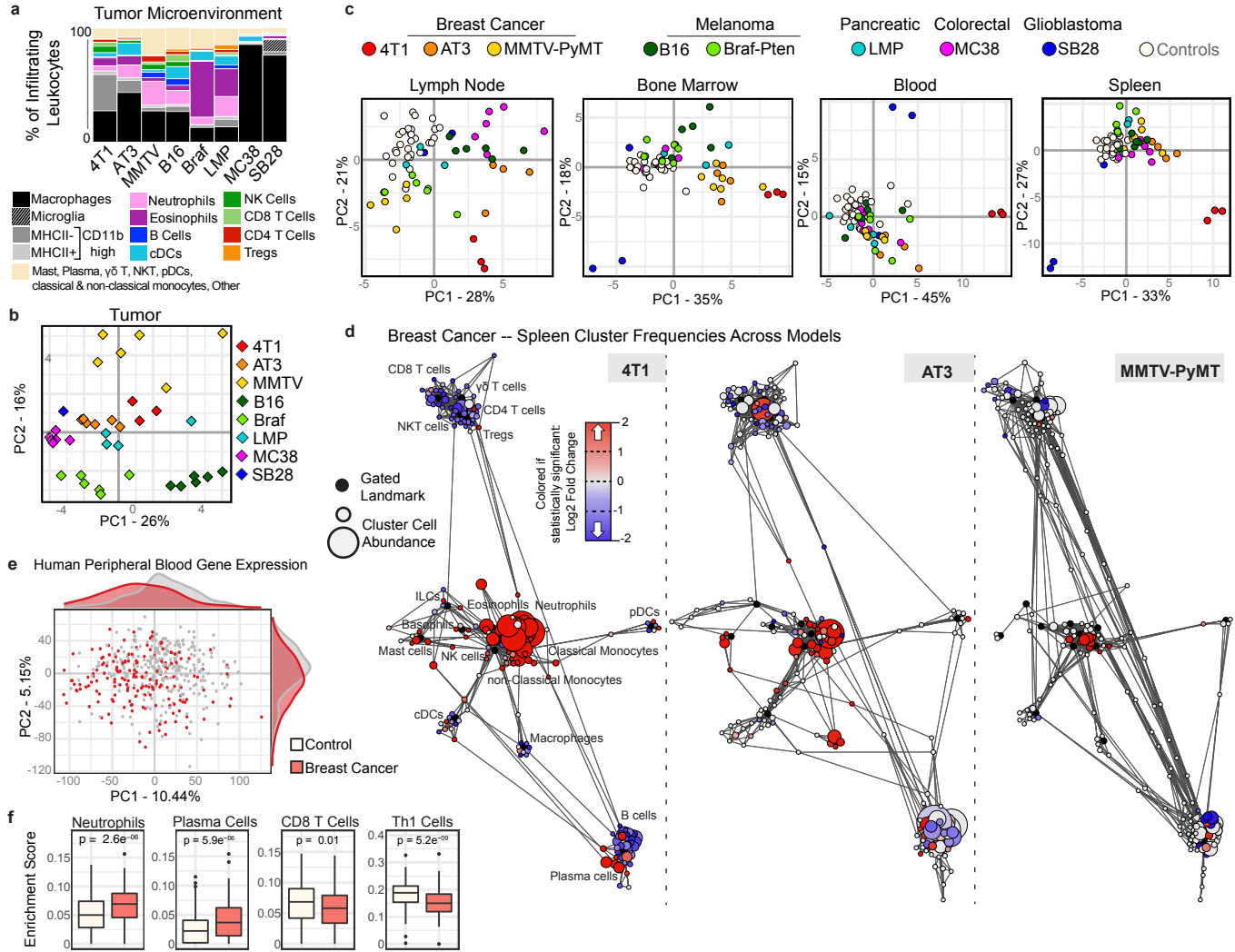




**Fig. 2: The systemic immune landscape is remodeled progressively over time.**

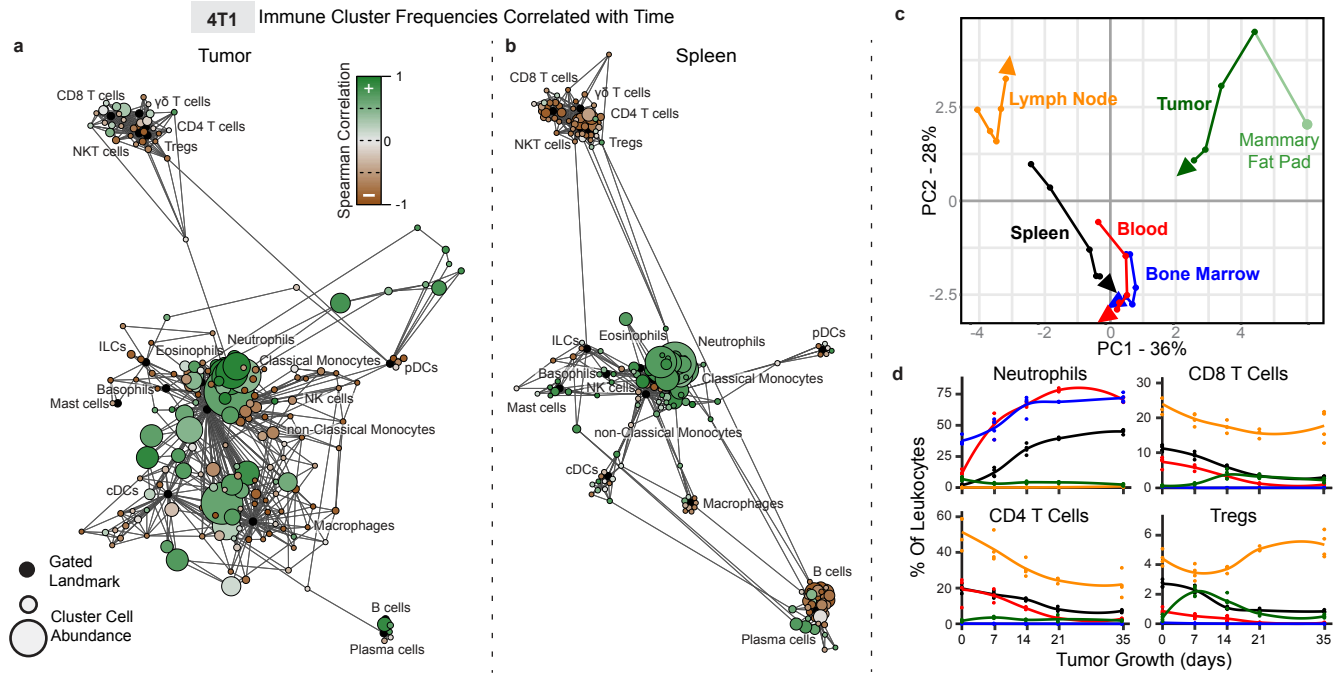


**Fig. 3: Tumor burden progressively changes systemic T cell composition.**

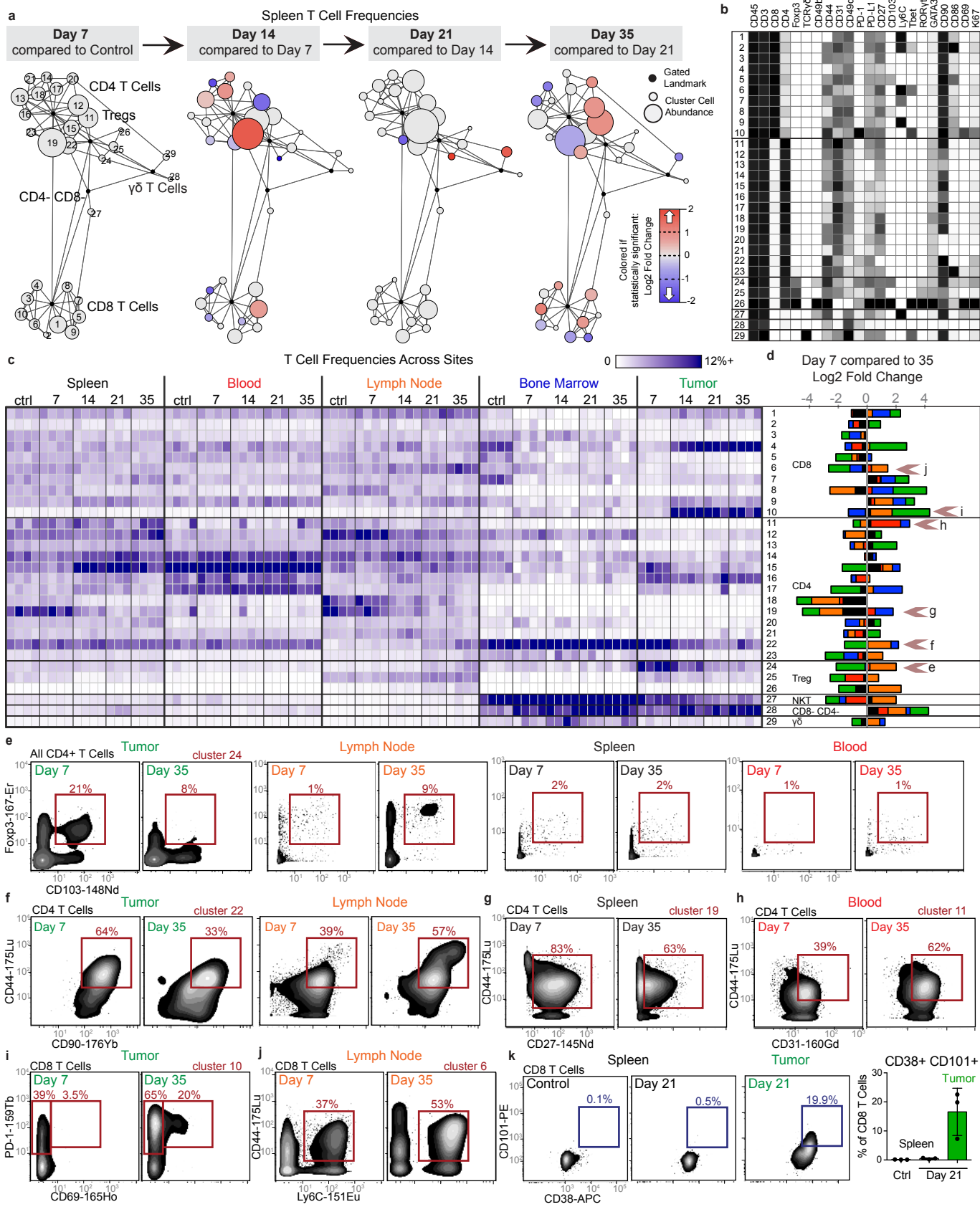


**Fig. 4: Tumor burden leads to impaired T cell responses to secondary infection.**

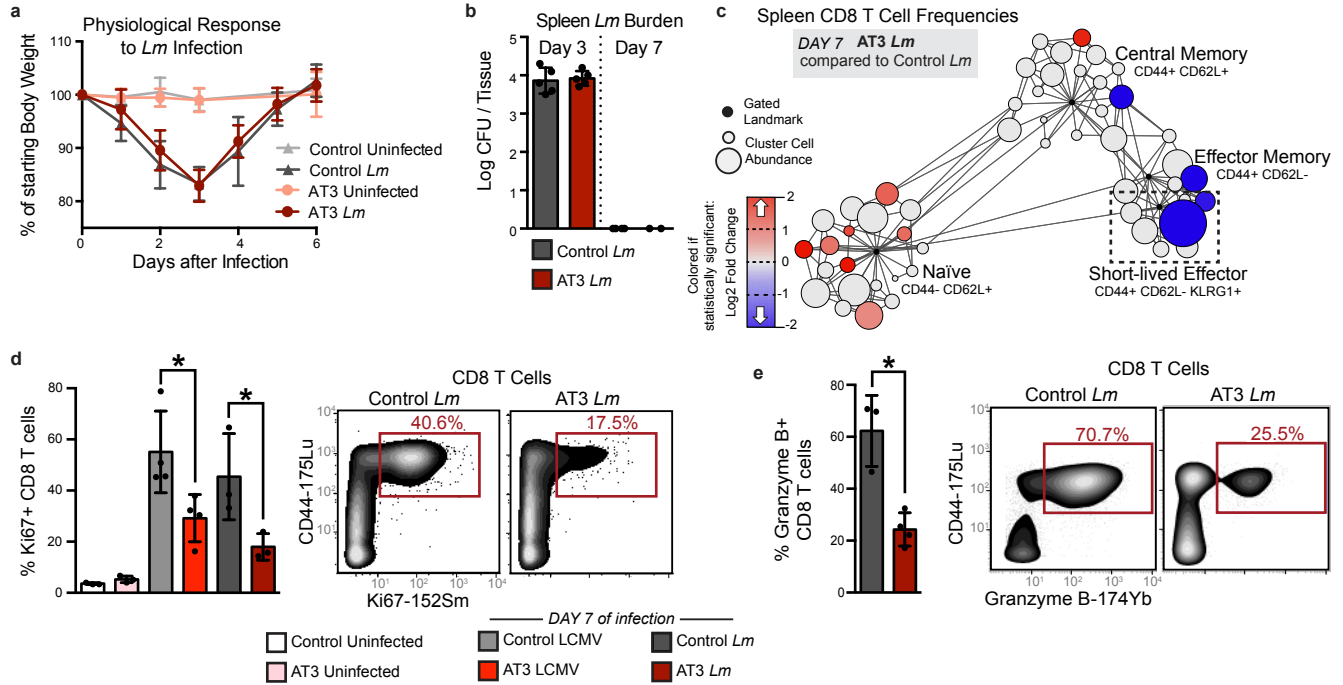


**Fig. 5: Tumor burden attenuates dendritic cell activation during secondary infection.**

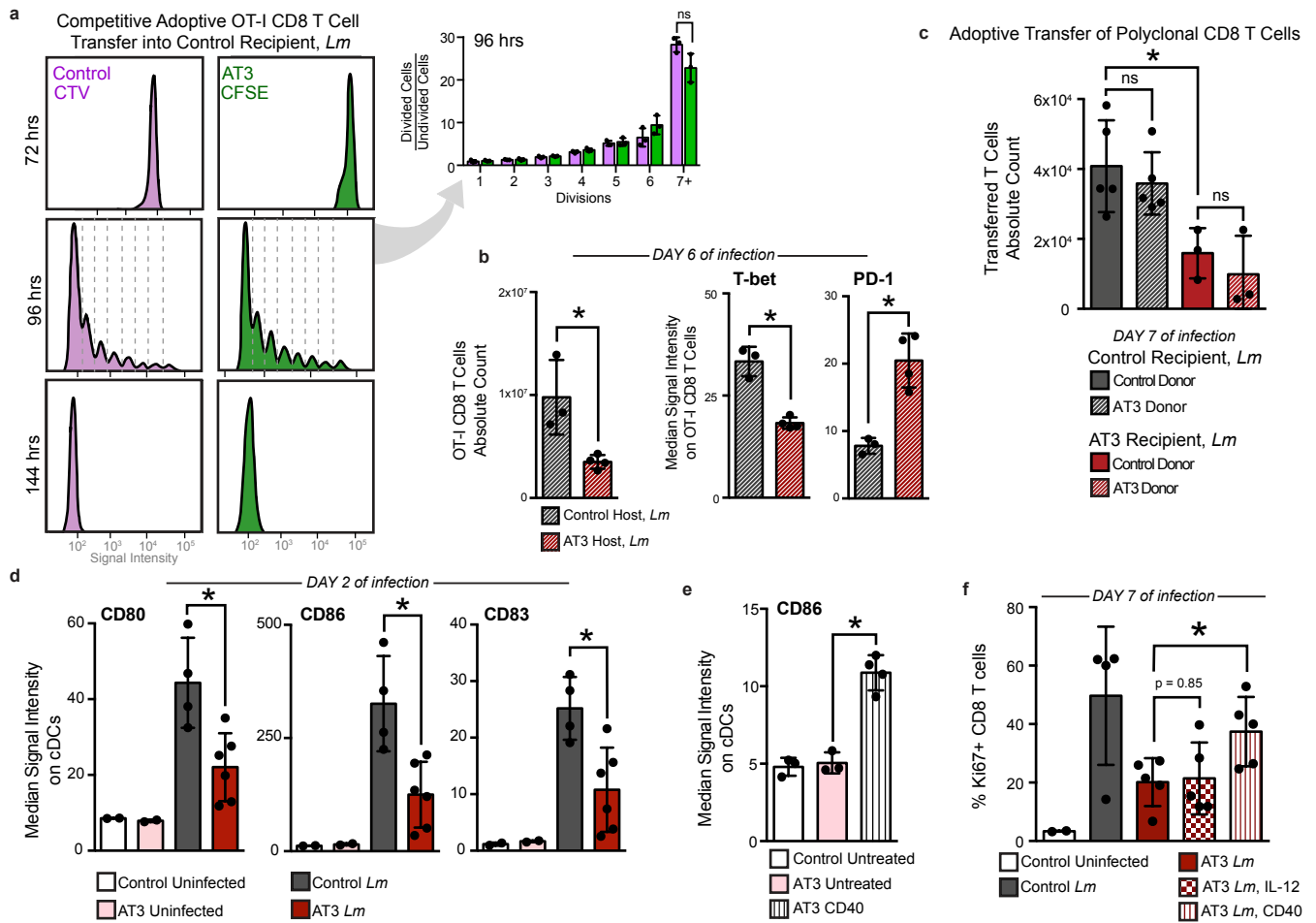


**Fig. 6: Tumor resection completely resets the systemic immune landscape.**

